Ref. Ares(2025)9600924 - 07/11/2025

OPERA HPC

OPEn HPC theRmomechanical tools for the development of eAtf fuels

Deliverable D5.1 – Results of the verification activities

Version 1 – 05/11/2025

Funded by the European Union

Disclaimer

Views and opinions expressed are those of the author(s) only and do not necessarily reflect those of the European Union or of the European Commission. Neither the European Union nor the granting authority can be held responsible for them.

While this document has been prepared with care, the authors and their employers provide no warranty concerning the content and shall not be liable for any direct, incidental or consequential damages that may result from the use of the information, or the data contained in it. Reproduction is authorised provided the material is unabridged and the source is acknowledged.

Document type	Deliverable
Document number	D5.1 version 1
Document title	Results of the verification activities
Authors	I. Guénot-Delahaie (CEA), T. Barani (CEA), A. Scolaro (EPFL), M. Krstović (EPFL), K. J. X. Sturm (EPFL), D. Pizzocri (POLIMI), G. Zullo (POLIMI), A. Zayat (POLIMI), L. Luzzi (POLIMI), L. Verma (PSI), I. Clifford (PSI), M. Horton (UKNNL), Z. Hinds (BANGOR), M. Rushton (BANGOR), A. Arkoma (VTT)
Release date	05/11/2025
Contributing partners	CEA, EPFL, POLIMI, PSI, UKNNL, VTT
Dissemination level	PU

Version	Short description	PMO	Main author	WP leader	Coordinator
1	First release	S. de Grandis (Sintec) 05/11/2025	I. Guénot-Delahaie (CEA) 02/10/2025	L. Luzzi (POLIMI) 03/11/2025	B. Michel (CEA) 05/11/2025

Abstract

This deliverable presents the corpus of verification activities performed in Task 5.1 for the three open-source advanced computational tools addressing the thermomechanical behaviour of nuclear fuel elements considered in the OperaHPC project, i.e.: the MMM mesoscale code, the multiscale meshless SPH method-based prototype tool, and the OFFBEAT engineering fuel rod scale code, coupled with the SCIANTIX code. Intended as the first component of the key VVUQ&SA process towards their qualification for nuclear safety studies, these verification activities encompass comparison of computational results with analytical and/or manufactured solutions in simple configurations, as well as code-to-code comparison with existing advanced multidimensional fuel performance codes (ALCYONE, BISON, Falcon) developed and/or used by OperaHPC partners on specific case studies consistent with the applications targeted in WP7 for which those codes are validated against experimental data. Acceptance criteria are detailed and shown as met in general terms.

Table of contents

Glossary

ASN	Former French Nuclear Safety Authority (now ASNR)
CDI	Cumulative Damage Index
CERMET	CERamic METallic
CI	Continuous Integration
eAtf	enhanced Accident tolerant fuel
IFPE	International Fuel Performance Experiments
IP	Inter-Pellet
LOCA	Loss-Of-Coolant Accident
MMM	`MFEM-MGIS-MFront`
MOX	Mixed-OXide (fuel)
MP	Mid-Pellet
OFFBEAT	OpenFOAM Fuel BEhavior Analysis Tool
OperaHPC	OPEn HPC theRmomechanical tools for the development of eAtf fuels
PCMI	Pellet-Cladding Mechanical Interaction
PWR	Pressurised Water Reactor
REBEKA	REactor typical Bundle Experiment KArlsruhe
RIA	Reactivity-Initiated Accident
RMSE	Root Mean Square Error
RVE	Representative Volume Element
SPH	Smoothed Particle Hydrodynamics
UQ&SA	Uncertainty Quantification & Sensitivity Analysis
V&V	Verification & Validation
WP	Work Package

1 Introduction

The objective of this document is to summarize the achievements of Task 5.1. Abiding by the quality assurance purposes reported in [1], it successively presents the various verification tests and studies performed for the three open-source advanced computational tools addressing the thermomechanical behaviour of nuclear fuel elements considered in the OperaHPC project (developed within WP4) with a view to contributing to their qualification for nuclear safety studies:

- the `MFEM-MGIS-MFront`, shortened MMM, mesoscale code [2] developed by CEA,
- a multiscale meshless SPH method-based prototype tool developed by UKNNL,
- the OFFBEAT engineering fuel rod scale code [3] developed jointly by EPFL and PSI and coupled with the SCIANTIX code [4] developed by POLIMI.

Depending on the tool considered, the verification process aiming at determining if the model equations are solved in a broad sense correctly rely on two types of activities:

- comparison of computational results with analytical (when available) and/or manufactured solutions in simple configurations,
- code-to-code comparison with existing advanced multidimensional fuel performance codes developed and/or used by OperaHPC partners on specific case studies consistent with the applications targeted in WP7 for which those codes are validated against experimental data.

2 Verification of the MMM mesoscale tool

2.1 Mesoscale applications developed for the OperaHPC project

The `MFEM-MGIS-MFront` (MMM) tool [5] is a multipurpose finite element solver tackling non-linear mechanic problems, combining the capabilities of the code generator `Mfront` [6] and the massively parallelized solver MFEM [7] thanks to the MGIS [8] layer. Each brick constituting the MMM code is subject to a strict quality assurance protocol, including the verification of the available numerical solvers, capabilities, and material property integrators: their presentation lies outside the scope of this work. Here we focus only on the verification of the applications built on top of the MMM software stack in the framework of OperaHPC, tailored to study the mechanical behaviour of nuclear fuel leveraging advanced computational tools.

Three study cases are considered in the project [9] and tackled with MMM. The first one represents the viscoplastic behaviour of a polycrystalline microstructure of UO_2, notably to reproduce the mechanical behaviour observed in compression creep tests. The second one studies the over-fragmentation induced by a population of pressurized spherical bubbles on UO_2 nuclear fuel in transient conditions. Finally, the third case represents a CERMET polycrystalline UO_2 with a chromium metallic interface expected in eATF fuels. The objective of this third case is to assess the mechanical state and potential over-fragmentation under high strain rates loading, representative of RIA conditions.

2.2 Verification tests

The specific verification tests used for the three MMM's applications of OperaHPC are detailed in Table 1. They are available and documented in [10], with more details for Case 1, Case 2 and Case 3 in [11], [12] and [13] respectively. The mesh convergence study remains to be done.

Study case	Verification test	Reference result
Case 1 Viscoplasticity of polycrystalline UO_2	Macroscopic stress-strain curve	Cast3M simulation on the same mesh
	Mean stress and strain per grain	
Case 2 Pressurized spherical bubbles in a porous elastic material	Local stress distribution	Analytical solution for a single bubble in an infinite media
	Stress interpolation between integration point and mesh nodes	Cast3M simulation on the same configuration
Case 3 Viscoplasticity of a CERMET polycrystalline UO_2	Macroscopic stress-strain curve	Cast3M simulation on the same mesh
	Mean stress and strain per grain	

Table 1 – Verification tests used for the MMM application of the OperaHPC project. Acceptance criteria: relative error < 1%.

2.2.1 Viscoplasticity of polycrystalline UO_2

The verification is based on simplified geometry with a compression test on a 5-grain polycrystal. The same Finite Element mesh (see Figure 1) is used with the Cast3M code (the reference solution) and the MMM application in order to enable a detailed comparison of the results including the mean strain and stress per grain. The crystal viscoplastic model is implemented in both codes with the same `MFront` file using the UO_2 law proposed in reference [14].

The macroscopic stress strain curves are compared in Figure 1 with a relative error[1] lower than 0.6 %. For the mean stress and strain per grain, the verification against the Cast3M solution leads to a relative error similar to the one observed for the macroscopic stress and deemed acceptable since lower than 1 %. The Von Mises stress plotted at the end of the loading in Figure 1 shows the stress heterogeneity induced by the variation in grain orientation and the viscoplastic anisotropy of UO_2 single crystal.

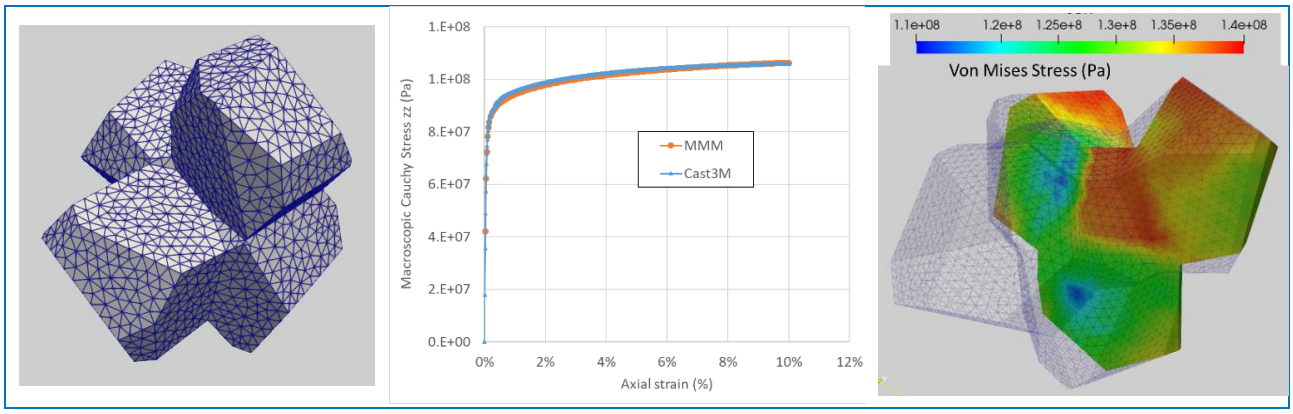

Figure 1 – Viscoplastic behaviour for a 5-grain polycrystal: (left) Finite Element mesh, (middle) stress-strain curve for a temperature of 1600 K and a strain rate of 5 x 10^{-4} s^{-1}, (right) Von Mises equivalent stress distribution at the end of the loading.

2.2.2 Pressurized spherical bubbles in a porous elastic material

The test case is dealing in general with a random distribution of monodispersed (empty) spheres into a periodic representative volume element (RVE), which is modelled as a perfectly elastic medium. A boundary condition of pressure is uniformly applied to the internal surface of the spheres, representative for the mechanical load induced by fission gas bubbles in the microstructure of UO_2. Since we do not have a reference analytical solution available for a complete simulation, given the intricate stress field resulting from the superposition of all the bubble contributions, we consider as a verification of the case the analytical solution of the stress field induced by a pressurized, spherical bubble into an infinite medium.

For a spherical cavity under internal pressure in an infinite elastic medium, we can exploit the spherical symmetry of the problem. The displacement field has only a radial component $u_r(r)$, and the problem reduces to solving the equilibrium equation in spherical coordinates. The equilibrium equation in spherical coordinates, considering only radial stress variations, is:

$$\frac{d\sigma_{rr}}{dr} + \frac{2(\sigma_{rr} + \sigma_{\theta\theta})}{r} = 0 \tag{1}$$

For an isotropic elastic material, the stress-strain constitutive relationships are:

$$\sigma_{rr} = \frac{E}{(1+\nu)(1-2\nu)}\left[(1-\nu)\varepsilon_{rr} + \nu(\varepsilon_{\theta\theta} + \varepsilon_{\phi\phi})\right] \tag{2}$$

$$\sigma_{\theta\theta} = \sigma_{\phi\phi} = \frac{E}{(1+\nu)(1-2\nu)}\left[\nu\varepsilon_{rr} + (1-\nu)\varepsilon_{\theta\theta}\right] \tag{3}$$

where E is the Young's modulus and ν is the Poisson ratio. The strain tensor components in spherical coordinates are:

$$\varepsilon_{rr} = \frac{du_r}{dr} \qquad \varepsilon_{\theta\theta} = \varepsilon_{\phi\phi} = \frac{u_r}{r} \tag{4}$$

[1] Defined here as the following arithmetic mean $\overline{(|sg\_MMM - sg\_Cast3M|/|sg\_Cast3M|)}$ over the nodes of the mesh.

Substituting the constitutive relationships into the equilibrium equation and using the compatibility conditions, we obtain a differential equation for the radial displacement. By considering the boundary condition at the bubble surface ($r = R_b$) of a uniform internal pressure p_{in}:

$$\sigma_{rr}(R_b) = -p_{in} \tag{5}$$

and working through the algebra, we can obtain the stress field. The final expressions for the stress components are:

$$\sigma_{rr}(r) = -p_{in}\frac{R_b^3}{r^3} \tag{6}$$

$$\sigma_{\theta\theta}(r) = \sigma_{\phi\phi}(r) = p_{in}\frac{R_b^3}{2r^3} \tag{7}$$

We reproduced the test case with MMM, by creating a computational mesh featuring a spherical bubble of radius 400 nm placed at the centre of a cubic RVE whose size is 10 µm. The mesh is made up of ~10^5 quadratic isoparametric elements with Lagrange shape functions, refined towards the sphere surface. A unitary internal pressure is considered in this simple test as the boundary condition for the surface of the spherical bubble, as well as periodic boundary conditions on the RVE with a null macroscopic deformation gradient. The solution obtained by MMM and the analytical one given by Eq. (7) for the tangential stress are compared in Figure 2 where it can be appreciated how the solution of the code is respecting the applied boundary condition on the bubble surface (relative error[2] lower than 5 %) and the decrease of the stress, proportional to the cubic distance from the sphere centre.

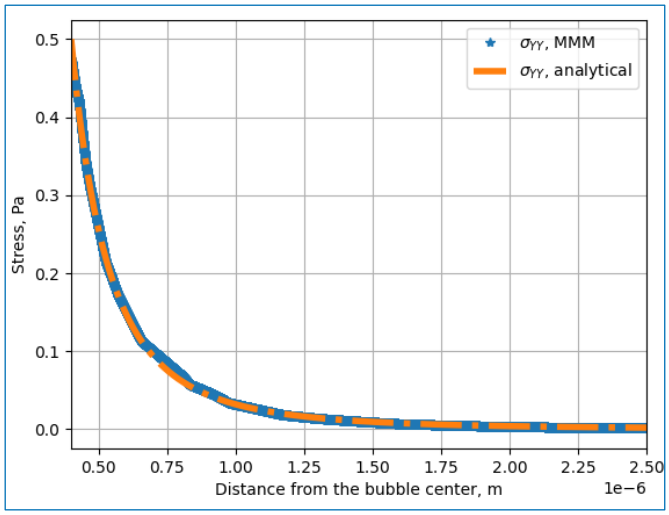

Figure 2 – Comparison of the analytical and the MMM solution for the stress field generated by a pressurized spherical bubble into an infinite elastic medium.

2.2.3 Viscoplasticity of a CERMET polycrystalline UO_2

The verification is based on simplified geometry with a compression test on a 5-grain polycrystal with a metallic interface located at grain boundaries. The same Finite Element mesh (see Figure 3) is used with the Cast3M code (the reference solution) and the MMM application in order to enable a detailed comparison of the results including the mean strain and stress per grain and in the metallic interfaces. In addition to the crystal viscoplastic model used for study case 1, the Norton law of Eq. (8) has been implemented with the MFront tool for the metallic interfaces.

[2] This value is based on an interpolation of the stress tensor to the nodes of the mesh. The discrepancy with respect to the value of the stress at the quadrature point closer to the surface is less than 1 %.

$$\dot{\varepsilon}_{eq} = \frac{A}{b^2} D_0 \exp\left(-\frac{Q}{RT}\right)\left(\frac{\sigma_{eq}}{C}\right)^n \quad (8)$$

The numerical values of material parameters given in Eq. (8) and the isotropic elastic properties of the Chromium interface are given in Table 2.

Parameter	Value	Parameter	Value
A	2.5×10^{11}	C	$264110 - 10\,T - 0.025\,T^2$
n	4.75	R	8.314
Q	306.27×10^3	E	$276.10^3\ MPa$
D_0	1.55×10^{-5}	ν	0.3
b	2.5×10^{-10}		

Table 2 – Material parameter values for the chromium metallic interface (unit system: s^{-1}, MPa, K).

The macroscopic stress strain curves are compared in Figure 3 with a relative error[1] lower than 0.2 %. For the mean stress and strain per grain, the verification against the Cast3M solution leads to a relative error similar to the one observed for the macroscopic stress and deemed acceptable since lower than 1 %.

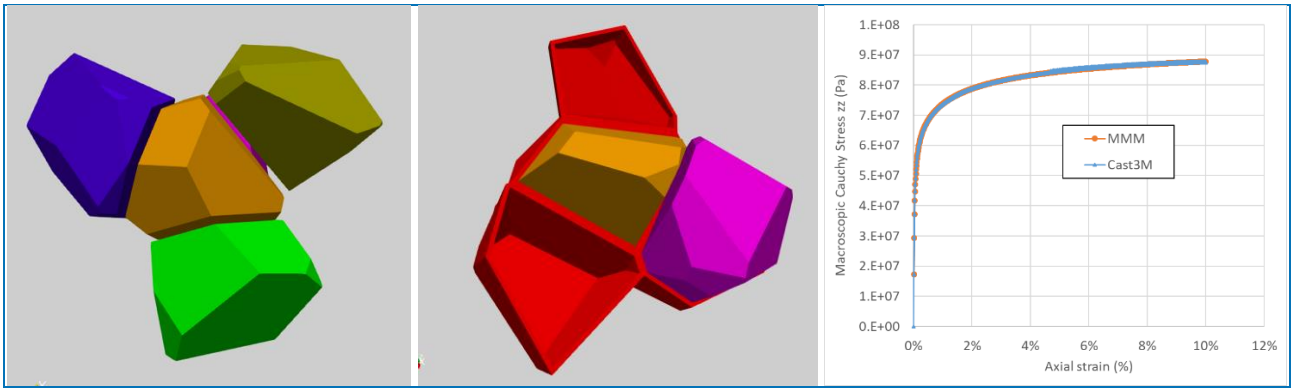

Figure 3 – Viscoplastic behaviour for a 5-grain polycrystal with metallic interfaces: (left) 5 grains without the interface, (middle) metallic interface in red and 2 grains, (right) stress-strain curve for a temperature of 1600 K and a strain rate of 5 x 10^{-4} s^{-1}.

3 Verification of the meshless SPH method-based prototype tool

SPH is a meshless continuum method which works by introducing a set of interpolation points (known as particles) instead of the usual mesh used by methods such as Finite Element Method. These particles are usually introduced in regular patterns (all work presented in this section uses grids) with some uniform particle spacing dp. Continuum material values are assigned at the interpolation points and then these are continuously interpolated within in any region based on a summation over the particles weighted by a gaussian-like smoothing function. It is important for verification therefore that the convergence of the method is confirmed and any interpolation errors are identified, particularly at system boundaries where less particles are included within the smoothing function summation.

The prototype SPH tool was created by modifying an existing SPH implementation (Smooth Mach Dynamics) within the LAMMPS software [15]. A series of extra functionalities were developed within the code to allow for prototype simulations of fuel fragmentation and relocation to be explored – specifically for the bottom of the fuel column, as they are not achievable with MMM and OFFBEAT –. These functionalities include

thermal conduction, convective boundary conditions, heat source terms and thermal expansion. For each functionality, code verification against analytical solutions was completed.

One example case for the analytical solution for the radial heat flux $\mathrm{Q_r}$ through a 2D annulus at radius r with inner i and outer o surfaces held at constant temperature T and a given density ρ and thermal conductivity κ is given in equation (9). The results for the steady state solution are shown in Figure 4 for a particle spacing $dp = 0.2$ mm. The verification work highlights a known issue within the SPH method [16] which is error introduced through boundary treatment and calculation methods.

$$Q_r = -\frac{\kappa}{\rho}\frac{T_o - T_i}{r ln\left(\frac{r_o}{r_{in}}\right)} \tag{9}$$

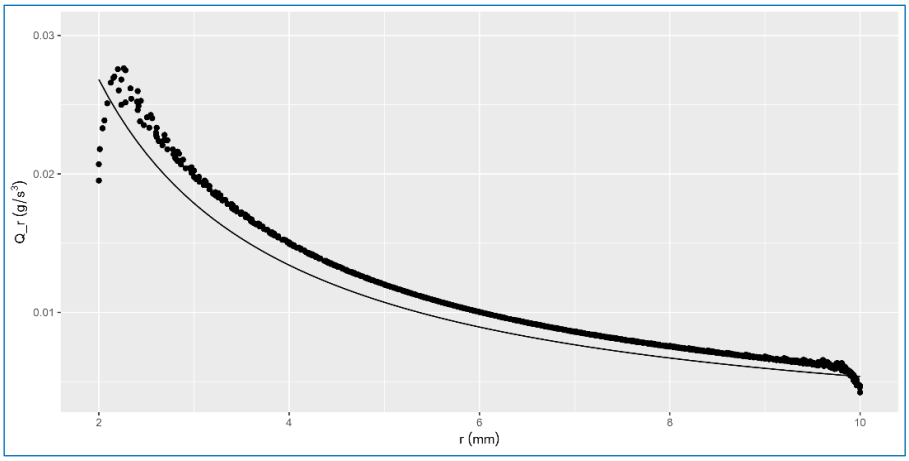

Figure 4 – Radial heat flux predicted by the LAMMPS SPH implementation (shown by the points) compared to the analytical solution (solid line). Generic values of $\kappa = 0.1$ gmm/Ks^3, $\rho = 3$ g/mm^3, $T_i = 1$ K, $T_o = 0$ K.

For nearly all verification cases boundary conditions used were fixed. The exception is for the convective boundary conditions implemented based on previous work [17]. Transient verification cases were used where possible including within the verification of the convective boundary conditions, an example of which is shown within Figure 5 for $dp = 0.2$ mm. An improvement in accuracy due to the boundary implementation can be seen in Figure 5 at the right most system edge where the SPH solution aligns with the analytical solution which is otherwise not observed with the divergence of the heat flux at the system boundary's seen in Figure 4.

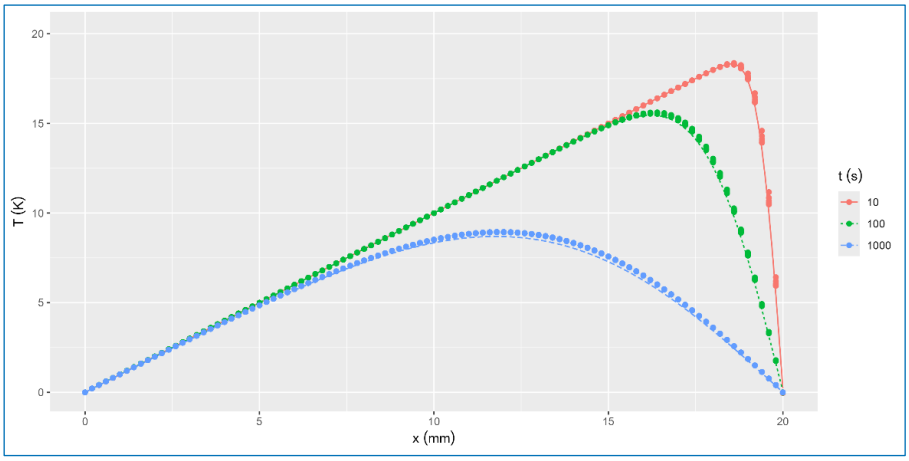

Figure 5 – Temperature profile for a material with left side at constant temperature and right convection heat with a coefficient of convection h= 2 g/Ks^3. Generic values of $\kappa = 0.1$ gmm/Ks^3, $\rho = 3$ g/mm^3, $T_\infty = 0$ K, $T_{x=0} = 0$ K.

The importance of boundary formulation on the error in simulation results can further be seen from the results for the annular thermal induced stress case shown in Figures 7 and 8. This is identical to the test case outlined for Figure 4 however a material thermal expansion coefficient $\alpha = 0.0001$ K^{-1} is introduced. The analytical solution assumes no radial stress at the material boundaries. In practice to achieve this the material at the boundary is free to move however a constant temperature is imposed within the inner and outer 0.5 mm of material (as shown in Figure 6). This introduces discontinuities in the heat flux which accompanied with the reduced number of particles included within the weight function at the system boundaries causes the largest error to occur at the boundaries.

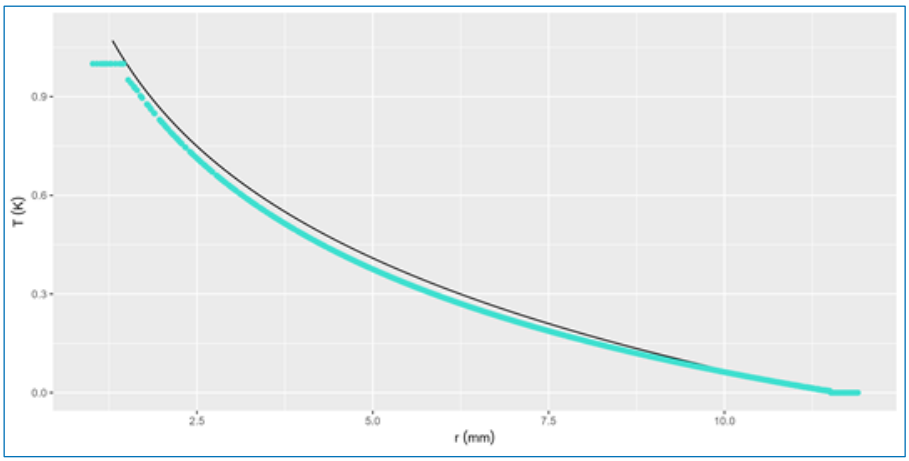

Figure 6 – Temperature results compared with the analytical solution for thermal induced stress in an annulus.

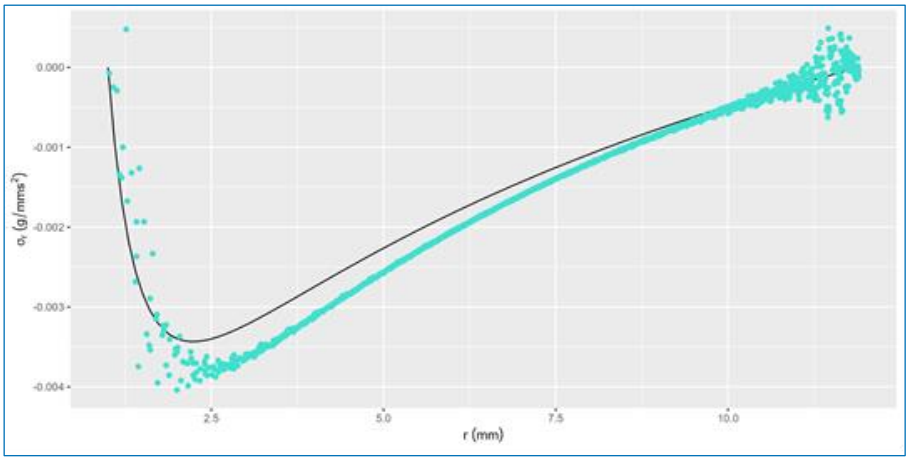

Figure 7 – Radial stress results compared with the analytical solution for thermal induced stress in an annulus.

Figure 7 shows a spread of particle results close to the boundary. This artifact is due to the non-uniform thermal expansion of material causing some compressive forces due to discretisation. This can be mitigated by introducing artificial viscosity terms, a common practice for smooth particle methods and by varying the mesh geometry (for all cases a square lattice was used, however concentric particle rings can give better results for annular geometries).

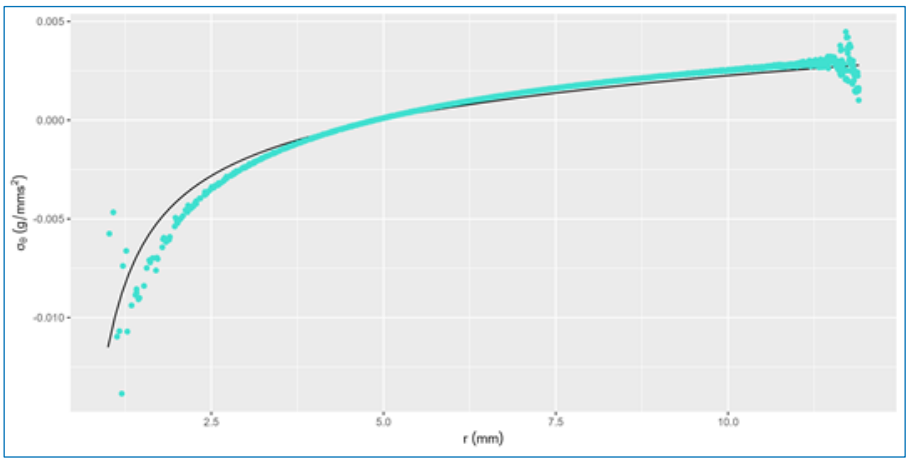

Figure 8 – Tangential stress results compared with the analytical solution for thermal induced stress in an annulus.

All verification test cases performed (see Table 3) were done across a variety of time steps (for transient cases) and across a range of particle spacing in order to demonstrate the calculations were convergent. Further information about each of the verification cases will be included within the release documentation for the tool under OperaHPC deliverable D4.3.

Analytical test case	Number of time steps	Number of particle spacings	Quantities tested	Order of convergence
1D transient heat flow	3	8	T	0.59-0.97
			Q	0.24-1.44
1D thermal induced stress	1	8	T	0.44
			Q	0.73
			σ	0.44
1D transient convection	3	8	T	0.17-0.91
			Q	0.91-1.61
1D heat source with constant boundary temperature	3	8	T	0.25-0.78
			Q	0.13-0.75
2D annular heat flow	1	8	T_r	1.02
			Q_r	0.74
2D annular thermal induced stress	1	8	T_r	0.61
			Q_r	2.80
			σ_r	0.93
			σ_θ	0.88

Table 3 – All analytical verification tests conducted on the prototype SPH tool. The convergence results are considered acceptable as the method is not divergent.

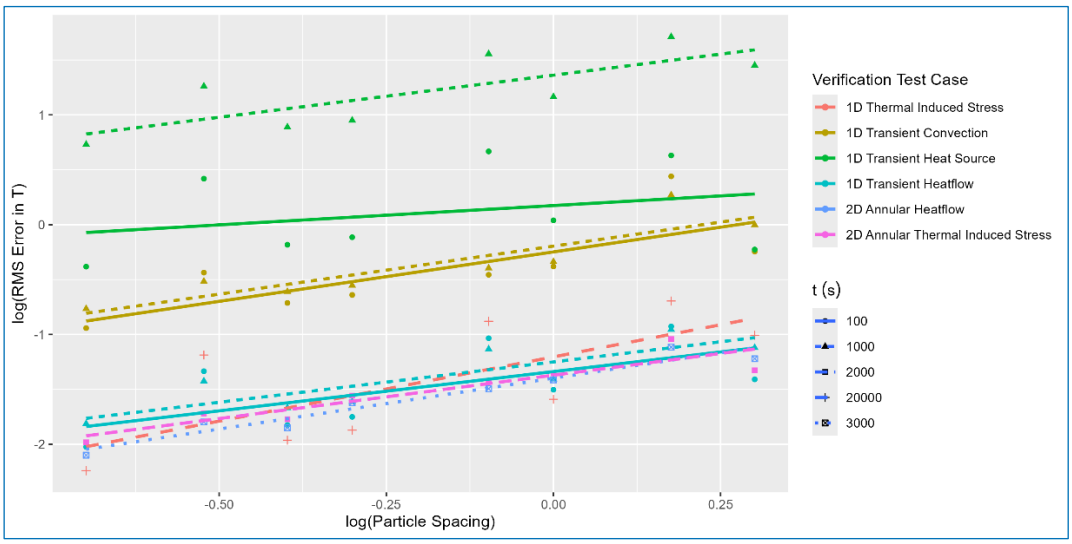

Figure 9 – Log of RMSE in predicted temperature profiles across a range of verification test cases compared to the expected analytical solution. Tests were performed for a range of particle spacing with the convergence behaviour for each test highlighted by linear fits.

Figure 9 shows the convergence for solutions of temperatures compared to the analytical solutions. Calculated RMSE values vary significantly as the particle spacing is reduced with a general convergent trend but instantaneous increases in error for some particle reductions. This is due to the interpolation error at the boundary as the interpolation grid of particles is not restricted to a division of the simulation box length and therefore the interpolation error at the boundary shifts dependent on the number of particles included within the summation for the smoothing function. The simulations were shown to be convergent for all cases examined. Figure 10 highlights that the order of convergence (calculated as the gradient of the linear fit of RMSE) observed was in general below 1. SPH is considered to be second-order accurate when considering the kernel smoothing length [18] however these findings align with often first-order reported convergence in practical applications due to the discretisation.

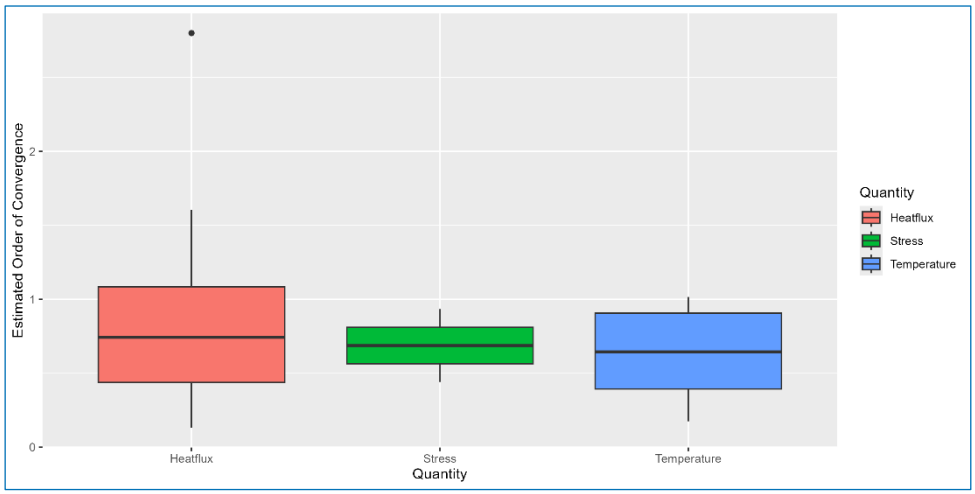

Figure 10 – Comparison of the spread of predicted orders of convergence for all verification tests completed across a range of variable (only radial stress is considered).

4 Verification of the OFFBEAT engineering fuel rod scale code

4.1 Verification of model implementation

Verification and Validation (V&V) have been integral to OFFBEAT since its inception. As the code expands in features, capabilities, and collaborative contributions, in particular within the framework of OperaHPC WP4, ongoing restructuring efforts aim to enhance reliability by aligning OFFBEAT with the V-Model framework [19], which is a systems engineering approach widely used in safety-critical industries such as aerospace, automotive, and medical devices. Its application to OFFBEAT is illustrated on Figure 11.

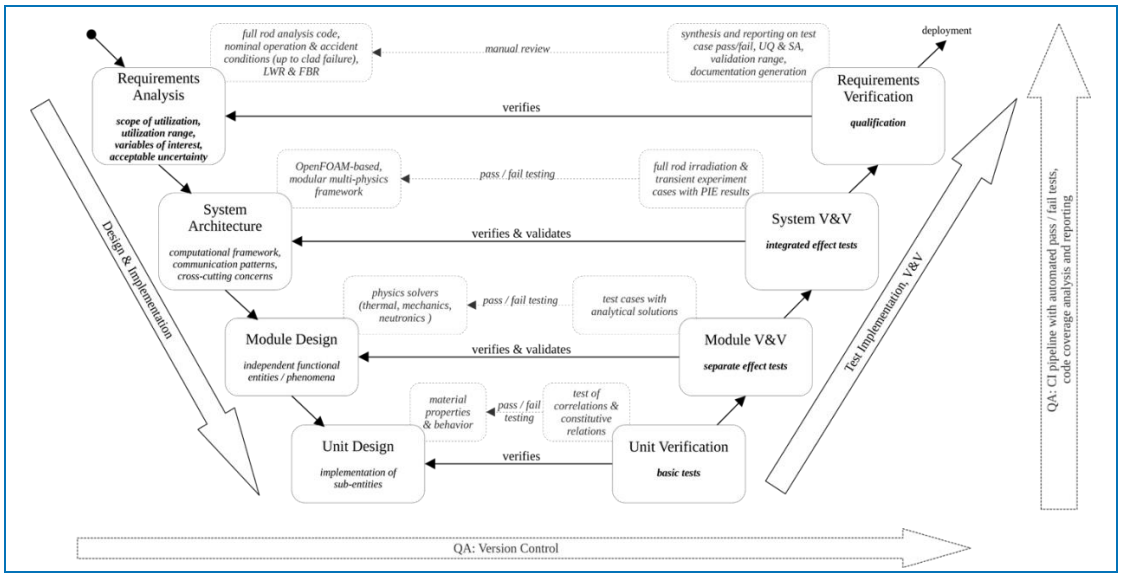

Figure 11 – V-Model and its application to the OFFBEAT development and V&V process.
Bold: Keywords from ASN Guide No. 28 [20]. Grey: Proposed implementation of V-Model phases for OFFBEAT. QA: Software assisted measures to support quality assurance.

The left branch represents the top-down development flow, beginning with high-level concepts and requirements, which are progressively refined into system architecture, modules, and individual units. The right branch follows a bottom-up testing path: each unit is verified through dedicated tests, then integrated into modules, which are also tested, culminating in full-system validation. This process ensures that both individual components and their interactions meet the original system requirements, enabling reliable deployment.

Basic tests (the lowest level in V-model hierarchy)

At the unit level, verification activities target the correctness of material properties and constitutive models. Each implemented correlation is being independently tested across its full intended parameter range and verified against publicly available reference data. To support this process, a standalone material verification utility has been developed. It reproduces model behaviour under defined input bounds and automatically compares the results to reference datasets.

Separate effect tests (the middle level in V-model hierarchy)

Separate effect tests verify individual solver modules (mechanical/thermal/neutronics solvers, and the implementation of boundary conditions) under controlled, simplified conditions. Configured as standalone cases with simple geometries, these tests isolate specific physical features. The figure of merit – such as stress distribution, temperature profile, interface stress, gap volume or others – varies depending on the case, but

in all verification cases it is compared against an analytical solution. With every major update, these tests are re-checked and, in most cases, only very minor deviations (below a pre-defined threshold) are expected. If the deviation exceeds the threshold, the underlying cause is systematically investigated.

The list of performed separate effect verification tests is presented in Table 4. All OFFBEAT verification cases are available in the GitLab repository [3] under the *Cases* folder.

Cases	Mechanics	Thermal	Material
Cantilever beam under load	X		
Plate with central hole under load	X		
Punch test	X		
Hoop stress test	X		
Thick cylinder expansion	X		
Large strain volume conservation	X		
Bi-material interface test	X		
Temperature and stress profile in fuel and cladding (steady-state & transient)		X	
Gap volume & heat flux conservation across gap		X	
Cladding corrosion layer growth and thermal resistance		X	X
Zirconium beta-phase transition			X
MOX fuel porosity migration			X
Hydrogen uptake, conservation, transport and reorientation			X
Transport of and heat removal by coolant		X	

Table 4 – Summary of separate effect verification tests.

Integrated effect tests (high level in V-model hierarchy)

Validation through integrated tests – including those based on the IFPE database [21] – represents the highest level in the V-Model hierarchy, assessing the full OFFBEAT code under realistic reactor conditions using experimental data. However, as this deliverable focuses exclusively on verification activities, these validation efforts will be addressed in future dedicated documentation within the OperaHPC project.

Furthermore, a continuous integration (CI) pipeline is being developed to automate routine testing and ensures code stability after each modification. This system will include automated test execution, coverage analysis, and generation of summary reports. These tools will ensure that new features are properly verified and validated, and that only reliable code is included in release versions.

4.2 Highlights from selected verification cases

As OFFBEAT's verification suite is extensive, this subsection showcases only a few representative cases from Table 4. A complete, per-case verification report will be published in the OFFBEAT GitLab repository once the CI pipelines are finalised for the next release under the OperaHPC project.

Tapered cantilever under shear

In this test, we reproduce the tapered-beam benchmark under transverse shear to verify bending–shear stress predictions (case IV of [22]). As shown in Figure 12, OFFBEAT matches the analytical bending stress along the z–y section (centreline in y) at multiple axial positions along the x-axis. Also, a magnified-warp contour confirms the expected shear-stress pattern.

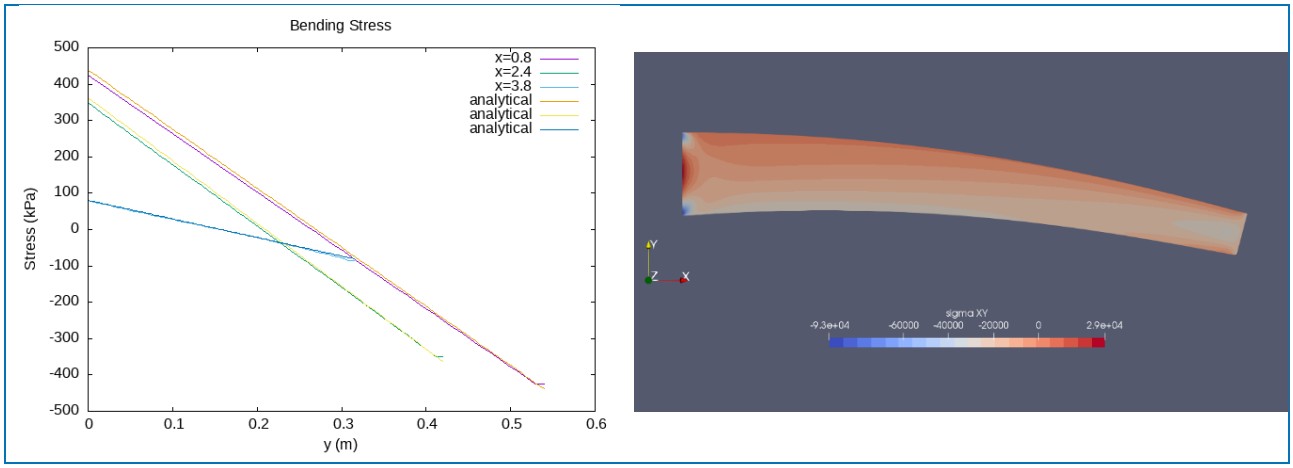

Figure 12 – (Left) Axial normal stress $\sigma_{xx}(y)$ across the z-y section (at z=0) at several locations along the x-axis: OFFBEAT *vs.* analytical. (Right) Shear stress σ_{xy} contours on the magnified-warp mesh.

LOCA verification I: thick-walled cylinder expansion (more information in [23])

In this test, we consider an axisymmetric 1D cylinder with inner/outer radii 10/20 mm. A prescribed inner-radius displacement ramps to 75 mm. Material data and case setup follow Cardiff *et al*. [24]. In Figure 13 (left side), the Updated-Lagrangian large-strain solver reproduces the analytical radial stress at the inner wall.

LOCA verification II: Zircaloy β-phase dynamic transition (more information in [23])
In this test we verify the Massih [25] dynamic phase transition model for Zircaloy (also available in BISON [26]) as implemented in OFFBEAT. The evolution of β-phase volume fraction predicted by the model is matched by OFFBEAT; Figure 13 (right side) shows the dynamic *vs.* static response for a case where the cladding segment is first heated and then cooled with a rate of $\pm$ 10 K/s.

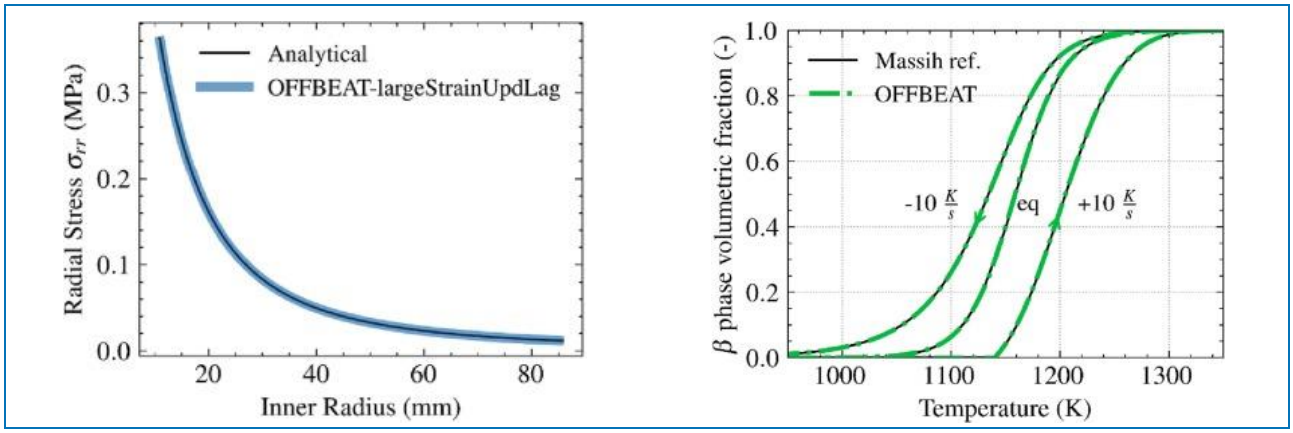

Figure 13 – (Left) Radial stress at the inner radius for the thick-walled cylinder expansion case: OFFBEAT *vs.* analytical. (Right) β-phase transition in Zirconium: OFFBEAT *vs.* Massih model (dynamic *vs.* static formulations).

Multi-material traction continuity

OFFBEAT's stress-displacement formulation for multi-material interfaces is checked for a variety of cases. Here we show the results for a bonded, infinite bi-material cylinder with different internal/external pressures across the two materials. Results show continuity of radial traction at the interface and the expected jump in hoop stress.

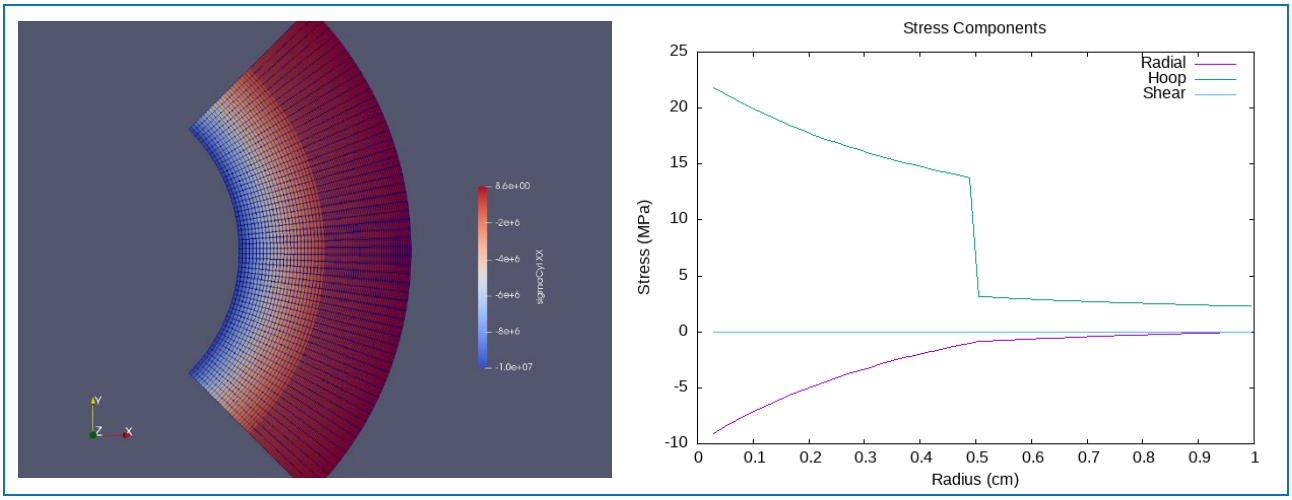

Figure 14 – (Left) Radial-stress contours. (Right) Radial profiles of stress components showing continuous radial stress and the expected discontinuity in hoop stress across the interface.

4.3 Focus on OFFBEAT-SCIANTIX scheme

In OFFBEAT [3][27][28], fission gas behaviour is modelled with SCIANTIX [4][29][30]. At each iteration and for every spatial discretization node, SCIANTIX gets from OFFBEAT local temperature, fission rate, and hydrostatic stress, and computes the volume concentrations (at/m^3) of relevant fission gases, e.g., xenon (Xe) and krypton (Kr), fission gas release and fuel gaseous swelling. As for the OFFBEAT-SCIANTIX coupling scheme, it is crucial to ensure an accurate numerical evaluation of the fission gas concentration, together with a low computational time. The quantity that mostly influences these two aspects is the intra-granular fission gas concentration, because it is the solution of a partial differential equation defined over spatial and temporal domains, namely, the geometry of the fuel grain and time. Fuel performance codes, as well as SCIANTIX, describe the intra-granular fission gas diffusion with the Booth equivalent sphere model [31] and the quasi-stationary assumption proposed by Speight [32]. Therefore, the resulting Eq. (10) describes gas diffusion in a spherical grain:

$$\frac{\partial c_t(r,t)}{\partial t} = D\left(T,\dot{F}\right)\frac{1}{r^2}\frac{\partial}{\partial r}\left(r^2\frac{\partial}{\partial r}c_t(r,t)\right) + \beta \qquad (10)$$

Numerical algorithms are available in literature, to handle Eq. (10), since the diffusivity is strongly non-linear. Examples include URGAS, FORMAS [33], PolyPole-1 [34] and PolyPole-2 [35]. Our reference algorithm is PolyPole-2, a spectral diffusion algorithm available in SCIANTIX. More details are available in [34][35]. The verification activity is carried out using the method of manufactured solutions (MMS) [36][37] which provides rigorous verification when the exact solution is not available. In SCIANTIX, an MMS framework for the intra-granular spectral diffusion solver has been added, enabling the user to specify a manufactured solution (c^M) and a manufactured diffusion coefficient (D^M). The solver then carries out verification by comparing its computed numerical solution (c^N) against the prescribed manufactured solution. Verification cases are available in the SCIANTIX repository [4]. Here, we report one representative case, with the selected manufactured solution shown in Figure 15, along with the corresponding verification steps. Note that c^M and D^M may be arbitrary functions of space and time.

$$c^M(r,t) = \alpha(a^2 - r^2)\sin(\varepsilon t) \quad ; \quad D^M(r,t) = \gamma \qquad (11)\,;\,(12)$$

The manufactured source term $\beta^M(r,t)$ is expressed by Eq. (13).

$$\beta^M(r,t) = \frac{\partial c^M(r,t)}{\partial t} - D^M\nabla^2 c^M(r,t) = \alpha\varepsilon(a^2 - r^2)\cos(\varepsilon t) + 6\alpha\gamma\sin(\varepsilon t) \qquad (13)$$

The manufactured source projection term then follows:

$$< \psi_k | \beta^M > = \beta_k^M = 2\sqrt{\frac{2\pi}{a}}\left(-\frac{6(-1)^k a^4 \alpha\varepsilon \cos(\varepsilon t)}{\pi^3 k^3} - \frac{6(-1)^k a^2 \alpha\gamma \sin(\varepsilon t)}{\pi k} \right) \quad (14)$$

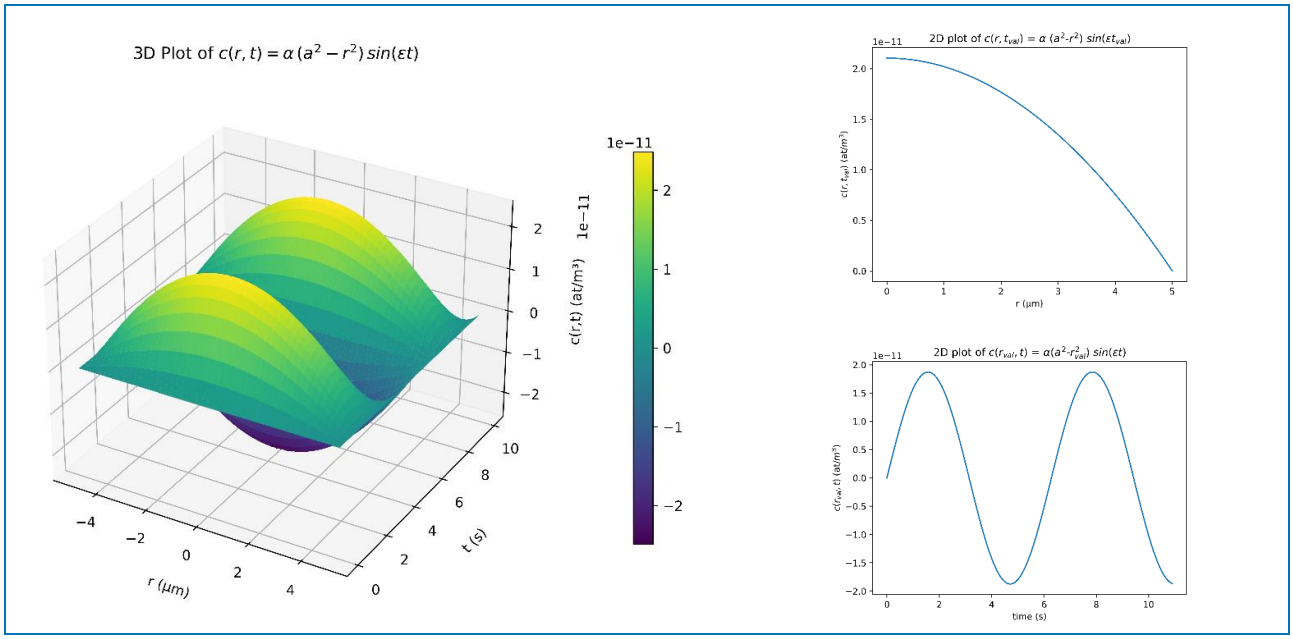

Figure 15 – Manufactured solution used for verification of the spectral diffusion solver. The left plot shows the full spatiotemporal profile $c^M(r,t) = \alpha(a^2 - r^2)\sin(\varepsilon t)$. The top-right plot displays the spatial profile $c^M(r, t_{val})$, illustrating the parabolic radial dependence at a fixed time. The bottom-right plot shows the temporal evolution of the concentration $c^M(r_{val}, t)$, demonstrating the sinusoidal behaviour in time of the analytical solution.

The results in Figure 16 show the qualitative agreement between the manufactured solution c^M and the numerical solution c^N calculated by SCIANTIX, for increasing number of modes and as a function of time. Figure 17 shows a similar agreement for the radial concentration profile. Figure 18 presents both temporal and spatial quantitative convergence studies.

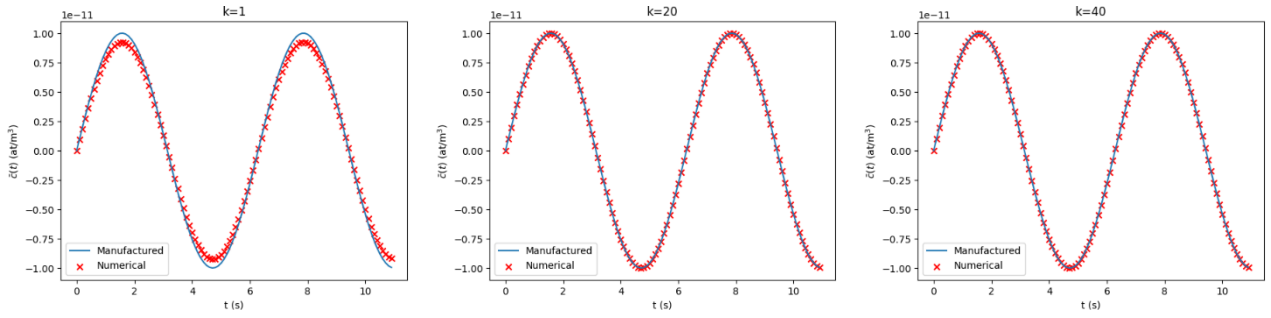

Figure 16 – Comparison between the manufactured solution c^M (solid blue) and the numerical spectral solver solution c^N (red crosses) for the volume-averaged concentration $\bar{c}(t)$ in the grain over time, for increasing mode number k.

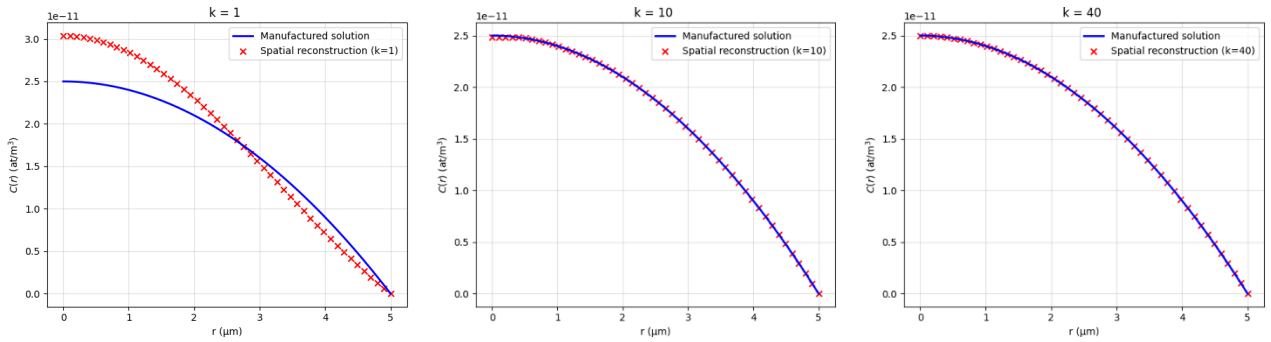

Figure 17 – Radial profile of the reconstructed concentration (red crosses) against the manufactured solution (solid blue line) using an increasing number of modes.

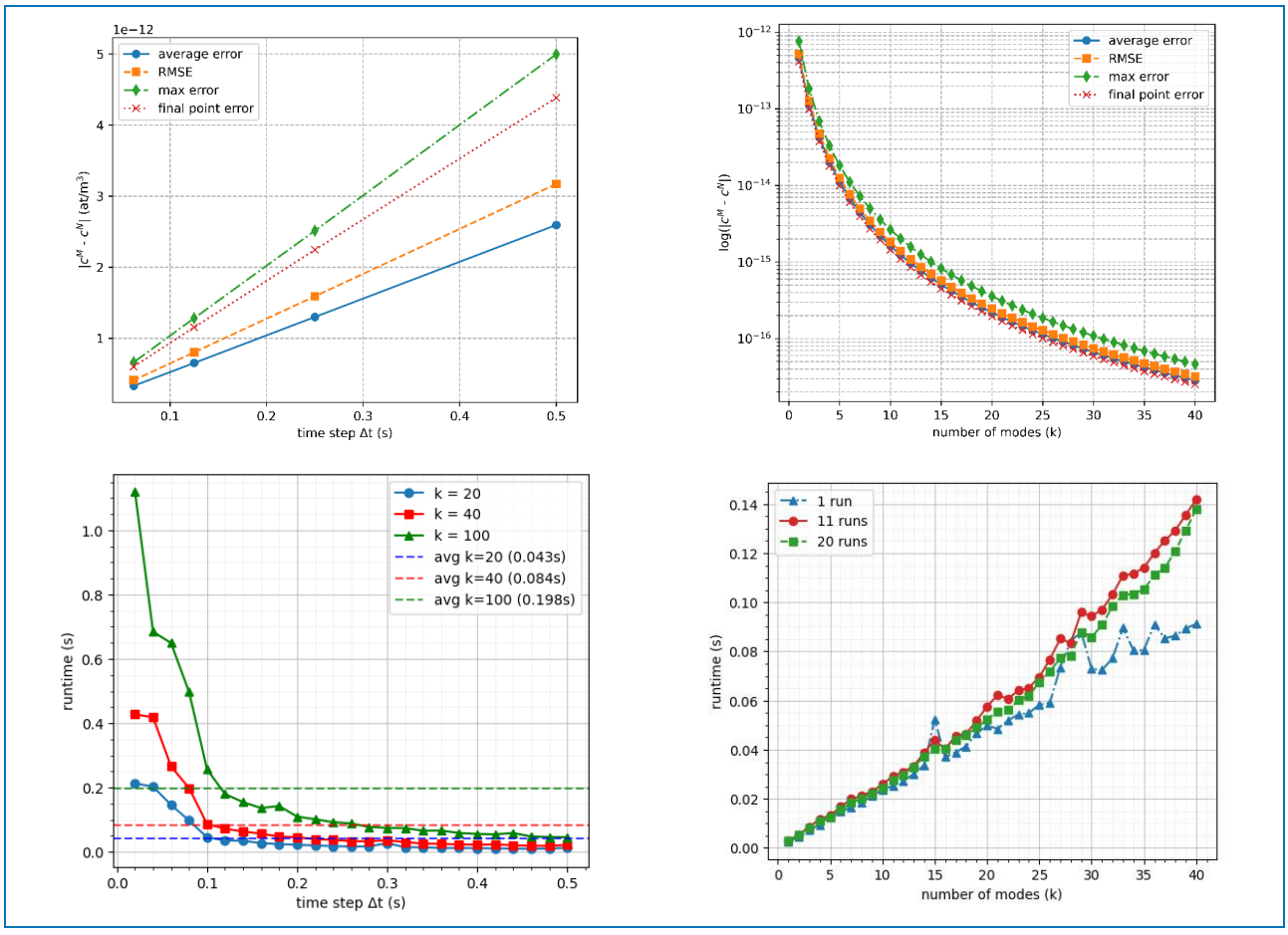

Figure 18 – Quantitative temporal and spatial convergence studies. Top-left: temporal convergence study showing error metrics $|c^M - c^N|$ versus time step Δt; all curves exhibit first-order accuracy, consistent with the implicit Euler scheme. A sufficiently high number of spectral modes ($k = 100$) is used to isolate the temporal error from the spatial one (left panel). Top-right: spatial convergence study demonstrating exponential decay of error with increasing number of spectral modes k. Bottom-left: runtime scaling with Δt for $k = 20$, 40, and 100, showing the increased cost of temporal refinement. Bottom-right: runtime scaling with number of modes k, illustrating the increase of the computational cost with increasing number of modes; the peaks are artifact due to random computational noise, as they tend to disappear over multiple averaged runs.

Figure 18 also shows that increasing the number of time steps requires greater computational effort. Increasing the number of modes from $k = 1$ to $k = 20$ reduces the error by nearly four orders of magnitude,

while going from $\mathrm{k} = 20$ to $\mathrm{k} = 40$ yields an additional reduction of almost two orders of magnitude (Figure 18, top-right). Notably, $\mathrm{k} = 20$ requires less than about half the runtime of $\mathrm{k} = 40$ (Figure 18, bottom-right). Currently, SCIANTIX handles 5 elements (3 stable and 2 non-stable), each projected onto 40 modes. Therefore, we improved the SCIANTIX code efficiency by using a hybrid approach for the mode allocation: we reduced the mode available for stable nuclides (Xe, Kr) from 40 to 20 modes, which preserves accuracy while cutting SCIANTIX runtime by 20–50 %. On the other side, non-stable nuclides (^{133}Xe and ^{85m}Kr) keep 40 modes, to capture their radioactive behaviour. As a result, the computational time of SCIANTIX and OFFBEAT coupled to SCIANTIX is roughly reduced by a factor two, preserving the numerical accuracy (cf. Table 5). This hybrid approach has been tested in the OFFBEAT working branch *development/sciantix2*.

% Relative error	40 modes	Hybrid approach
Average	3.702	3.702
RMSE	3.934	3.934
Max	4.985	4.987
Final	0.104	0.107

Table 5 – Relative error with respect to the manufactured solution for the intragranular fission gas concentration, for $\mathrm{k} = 40$ modes and the hybrid approach (20 modes for stable gases, 40 modes for short-lived radioactive gases). The relative errors of the two approaches differ roughly of about 0.05 %.

To extend the MMS to fission gas release, we illustrate here the results of using a fast oscillating manufactured solution (available in the SCIANTIX repository [4]). The gas at grain boundary is given by:

$$\frac{\partial c_{GB}}{\partial t} = J_{in} - R \tag{15}$$

Eq. (15) states that the evolution of the gas at the grain boundary is determined through the incoming flux from intragranular diffusion $\mathrm{J_{in}}$ and the release rate R. For this case, we neglect intra-granular irradiation-induced resolution and grain-boundary bubble evolution, i.e., once the gas reaches the boundary it is directly released. The corresponding results are presented in Figure 19. Similar results available in the SCIANTIX repository [4] have been obtained for the other quantity of Eq. (15), the gas at grain boundary c_{GB}, for the same fast-oscillating MMS.

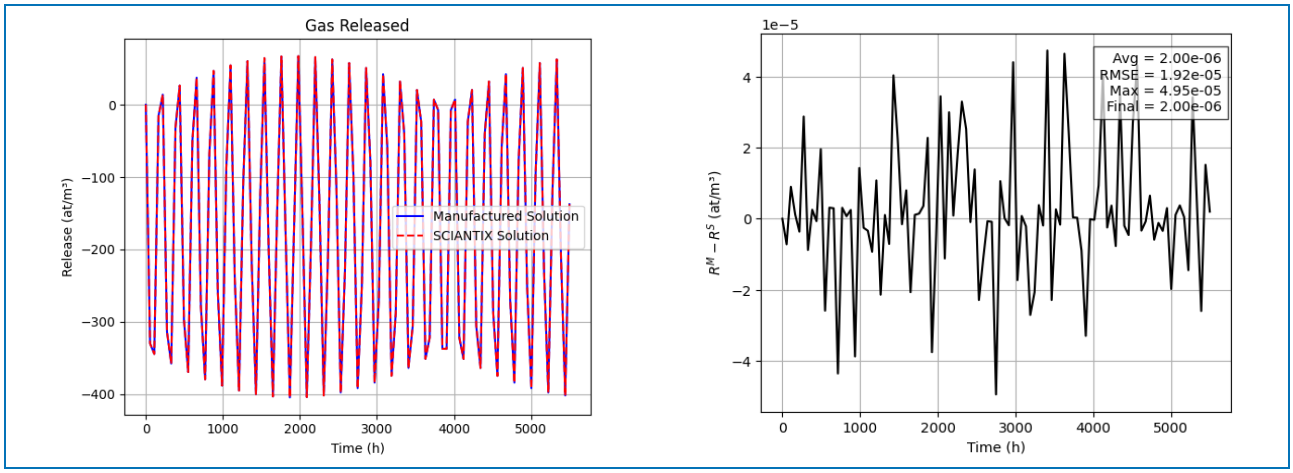

Figure 19 – Comparison between the manufactured solution (solid blue) and SCIANTIX predictions (dashed red) for gas release. Left: temporal evolution of the gas release as manufactured solution (blue) and calculated by SCIANTIX (red). Right: absolute error between the two solutions ($\mathrm{R^M} - \mathrm{R^S}$) with average, RMSE, maximum, and final error values annotated.

4.4 Code-to-code benchmarks

4.4.1 2D-3D ALCYONE-BISON-OFFBEAT benchmark

This work involves EPFL, CEA, and VTT, which report results using the codes OFFBEAT, ALCYONE [39], and BISON [40], respectively.

This benchmark focuses on the analysis of Pellet-Cladding Mechanical Interaction (PCMI) during base and a subsequent ramp irradiation. The evolution of cladding deformation and stress profiles is compared across the codes at selected time points. Fuel centreline temperature and gap width evolution are also analysed. The benchmark simulation case is inspired by the K11-5 rodlet experiment from the IFPE database [21]. To allow a more straightforward comparison between codes, the geometry and irradiation history were simplified.

The modelled rodlet consists of 10 dished oxide fuel pellets, undergoing two years of base irradiation, followed by refabrication and a 13-hour ramp irradiation at a terminal power level corresponding to a linear heat rate of 42 kW/m. A flat axial power profile is assumed. The gap pressure at the start of both the base and ramp irradiation phases is set to 2.6 MPa. The geometry of the simulated rodlet, applied material properties, as well as the detailed irradiation history can be found in the conference paper [41].

ALCYONE employs its multilayered 3D computational scheme with local 3D meshes, *i.e.* one quarter of an idealized 3D fuel fragment, subject to appropriate boundary conditions adopted for each pellet [42]. OFFBEAT and BISON model the full rodlet using a 2D axisymmetric discrete-pellet configuration, where a stack of dished pellets is represented as a thin circumferential wedge with the overlying cladding.

The expected and observed differences in PCMI predictions between the codes, primarily originate from their treatment of fuel cracking. By explicitly representing radial cracks through its 3D fragment scheme, ALCYONE naturally captures the pellet hourglassing induced by the thermal gradient. In contrast, 2D axisymmetric geometries rely on relocation models to represent the effective radius increase of the fuel pellet associated with its fragmentation and its hourglassing. OFFBEAT applies an isotropic cracking approach to represent stress relief due to cracking, while BISON uses an orthotropic smeared cracking model. In addition to explicitly modelling the fragment geometry, ALCYONE applies a smeared cracking model to capture stress relief from secondary cracking during the power ramp. As already mentioned, the largest pellet hourglassing is expected to be predicted by the 3D fragment modelling. However, in the case of 2D geometries, the orthotropy of the softening model leads to a more pronounced hourglass shape compared to the isotropic softening, which is also observed in the benchmark results.

Additionally, the observed discrepancies in centreline temperatures may be attributed to differences in the fuel thermal conductivity models. The specific models used by each code are summarized in Table 6, while corresponding references can be found in [41].

UO_2 model	OFFBEAT	ALCYONE	BISON
Relocation	FRAPCON	3D fragment modelling	Modified ESCORE model
Cracking (softening)	Isotropic cracking (Barani's model)	Smeared cracking	Smeared cracking with power law (fracture strength: 168 MPa)
Thermal conductivity	NFIR	Modified Lucuta's formulation	NFIR

Table 6 – Dominant physical models driving the differences between codes.

Figure 20 presents the evolution of the gap width during base and ramp irradiation. It is observed that BISON predicts delayed gap closure. During base irradiation, gap closure in ALCYONE is driven by cladding

creepdown and also by the pellet swelling, which includes the hourglass shape transformation of the pellet fragment leading to a gap closure starting at the inter-pellet (IP) plane and then progressing toward the mid-pellet (MP) plane during irradiation. As illustrated on Figure 21, the cladding diameter computed with ALCYONE shows the impact of the creepdown (see the negative radial displacement at the end of base irradiation) and of the pellet-cladding interaction induced by the pellet fragment hourglass shape (see the evolution of the cladding ridges during irradiation). In OFFBEAT, gap closure is driven by the same mechanisms with cladding creepdown and pellet swelling. However, a free strain – fuel relocation – is added in order to enhance the pellet diameter increase. The ALCYONE MP plane results are closer to the OFFBEAT predictions compared to those at the IP plane.

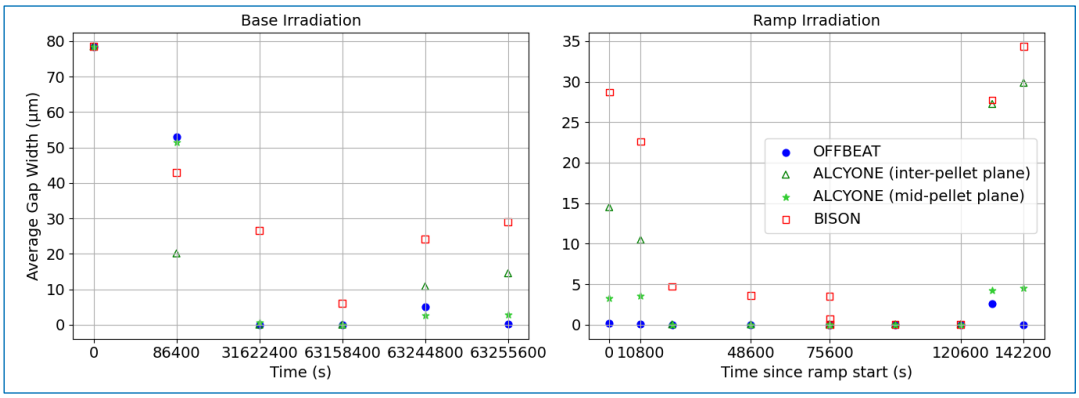

Figure 20 – Gap width evolution - OFFBEAT and BISON (averaged over the height), ALCYONE (corresponding to the IP and MP horizontal planes at the circumferential symmetry plane). Beware of non-linear time scale.

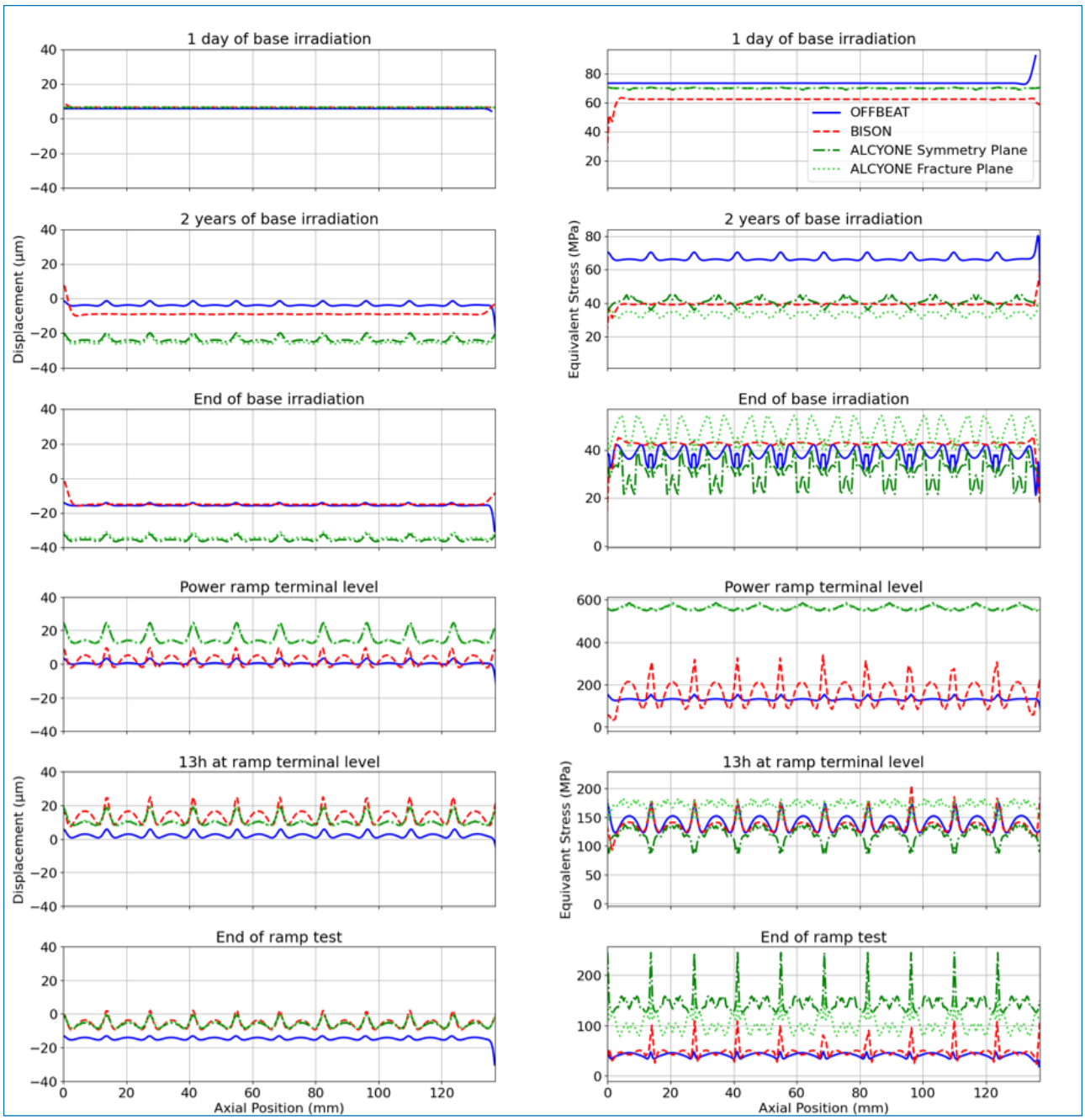

Figure 21 – Cladding radial displacement (left) and equivalent stress at the cladding inner surface (right) at six selected time points throughout the irradiation.

Base irradiation phase

ALCYONE predicts the most pronounced cladding creepdown (≈ -34 μm) by the end of base irradiation. This discrepancy with respect to OFFBEAT and BISON can be linked to the differences between the cladding creep laws used in the benchmark and to the fact that the pellet diameter evolution is increased by an empirical fuel relocation strain in OFFBEAT and BISON. OFFBEAT underestimates ridge height compared to ALCYONE, which can be attributed for the former to higher global fuel softening and the isotropic nature of its cracking model. BISON shows delayed gap closure, predicting lower fuel expansion and less cladding creepdown during base irradiation compared to other codes. This results in no ridges observed at the end of base irradiation for BISON.

Ramp irradiation phase

At the ramp terminal level, OFFBEAT and BISON predict similar average cladding displacements, while ALCYONE shows more than 15 µm larger outward displacement. This can possibly be due to higher fuel thermal expansion associated with higher centreline temperatures, and also to a different gaseous swelling. ALCYONE predicts significantly higher cladding stresses compared to OFFBEAT and BISON, driven by larger fuel expansion and the use of cladding hardening model. Over the duration of ramp irradiation, OFFBEAT predicts nearly constant average displacement (fuel is very soft), while ridges gradually increase. ALCYONE shows a slight decrease (~5 µm) in average displacement due to fuel and cladding creep, with stable ridge heights. BISON shows increased ridge formation and over 10 µm growth in average displacement, likely driven by enhanced swelling. This leaves ALCYONE and BISON with nearly aligned average displacements at the end of ramp irradiation. During post-ramp power-down, all three codes predict similar amount of cladding contraction.

Figure 22 shows the fuel centreline temperature evolution. Although OFFBEAT and BISON use the same fuel thermal conductivity model, BISON predicts higher temperatures during base irradiation due to the gap remaining open. During ramp irradiation, OFFBEAT and BISON predict very similar centreline temperatures. ALCYONE predicts higher fuel temperatures, exceeding OFFBEAT and BISON by more than 180 K during ramp irradiation. The higher temperatures in ALCYONE may be attributed to differences in the fuel thermal conductivity models. Reported temperatures correspond to the MP plane, approximately 70 K higher than the IP plane, slightly reducing the deviation from OFFBEAT and BISON.

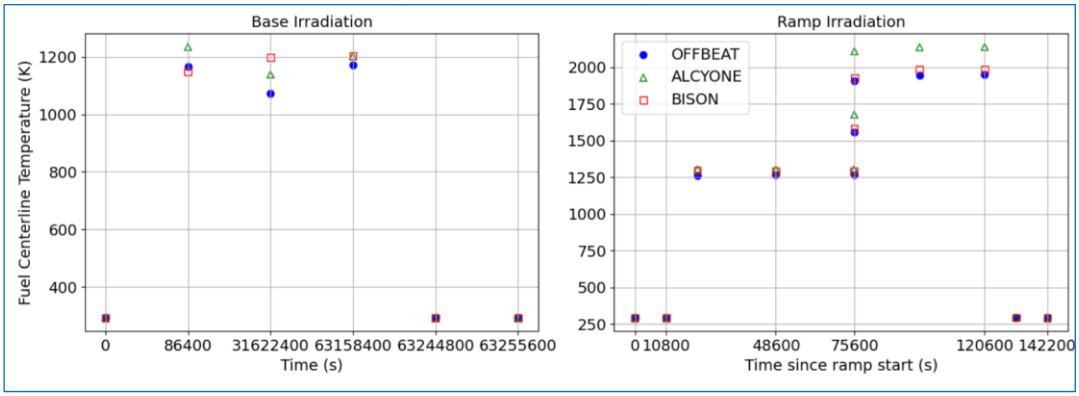

Figure 22 – Fuel centreline temperature evolution. Beware of non-linear time scale.

This PCMI benchmark confirms overall consistency among the codes, while also highlighting key differences and identifying their likely origins. They point to areas that warrant further investigation, such as cracking and relocation models, as well as the use of a unified set of material data for the benchmark.

4.4.2 2Drz Falcon-OFFBEAT benchmarks

Within this task, OFFBEAT validation cases on LOCA scenarios, carried out in Task 5.2, were compared with corresponding simulations using the Falcon [43] fuel behaviour code at PSI. For a code-to-code comparison, most of the models used in the two codes were kept the same, wherever possible. Some differences exist in the models available in the two codes, and the influence of these differences were investigated. Two validation cases for LOCA scenarios from Task 5.2 were used for the code-to-code benchmark of Falcon and OFFBEAT. These included the separate effect REBEKA test for cladding ballooning and burst and the MT4 material tests on integral rod during an adiabatic heat-up and reflood phases of a large-break LOCA. The Falcon-OFFBEAT code-to-code comparisons for these two cases are presented in the following sections.

4.4.2.1 REBEKA separate-effects tests for LOCA

The REactor typical Bundle Experiment KArlsruhe, REBEKA, separate-effects tests [44][45] are temperature transient tests in steam performed on single Zircaloy-4 cladding tubes used in PWRs at a variety of rod internal pressures and heating rates. The purpose of the tests was to analyze the cladding behaviour and obtain data of cladding ballooning and burst when subjected to LOCA conditions. The internal rod pressure was varied in a range of 1 to 140 bar for heating rates of ≈ 1 to 35 K/s. The information about the properties of the cladding tube is presented in the technical report KfK4343 [45] and further information can be found in [44]. It was noted that with the same heating rate, a higher rod internal overpressure results in a lower burst temperature and a higher heating rate leads to higher burst temperatures for the same rod internal pressure.

A 2D axisymmetric r-z geometry was used for the simulations using Falcon and OFFBEAT. The cladding surface was provided with the same axial temperature profiles. In Falcon, the Limbäck and Anderson creep model [46] is used for the standard temperature regime (same as in OFFBEAT) and the MATPRO creep model [47] in the high temperature regime. OFFBEAT on the other hand uses the Erbacher model [45] for high temperature creep. A total of 20 cases with rod internal pressure values in the range of 1-14 MPa and heating rates of 1, 10 and 30 K/s were used. The BISON results for these 20 cases from [48] were also compared with the Falcon and OFFBEAT results. The burst temperature *versus* internal pressure plots for OFFBEAT, BISON and Falcon for the heating rate of 1 K/s are presented in Figure 23 (a). The general trend of decreasing burst temperature with increasing internal pressure as well as increasing burst temperature with increasing heating rates is followed in all the three codes. With respect to OFFBEAT and BISON, the results from Falcon are significantly lower in all the cases, except for 1 and 2 MPa pressure cases.

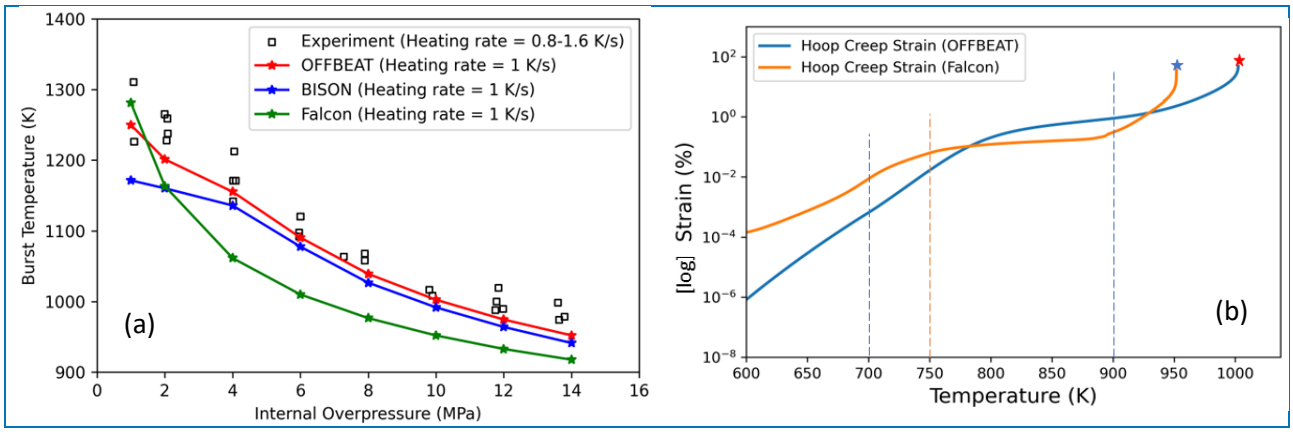

Figure 23 – (a) Burst temperature *vs.* internal overpressure, (b) hoop strain *vs.* temperature (adapted from [49])

For the 10 MPa pressure case, the temperature at burst using OFFBEAT was 1002.4 K and the time of burst was 693.54 s. On the other hand, for Falcon, moments before the point of failure the hoop creep strain was 35.52 %. The temperature at burst was 951.89 K and the time of burst was 642.90 s. The evolution of the hoop creep strain with temperature in Falcon and OFFBEAT is plotted in Figure 23 (b). The rise in hoop creep strain starts earlier in Falcon and thus, the cladding fails earlier, reaching lower burst temperatures than in OFFBEAT. The effect of the different high temperature creep models used in the two codes can be noticed. From the analysis, it seems that the different creep models for the high and intermediate temperature regimes used in Falcon and OFFBEAT lead to differences in the burst properties.

4.4.2.2 MT4 material test for LOCA

The IFPE/MT4-LOCA [50] test belongs to a series of thermal-hydraulic and cladding mechanical deformation tests conducted by the U.S.-NRC in the National Research Universal (NRU) reactor at the Chalk River National Laboratory in Canada. The MT4 test was aimed at providing sufficient time in the α-Zircaloy ballooning window of 1033 to 1200 K to allow the test rods to rupture before reflood cooling was introduced, obtaining data for cladding ballooning, and burst, and measuring the rod internal gas pressure during rod deformation. The MT4 test bundle simulated a 6x6 section of a 17x17 PWR fuel assembly containing 12 fresh pressurized tests rods. All but one rod failed during the adiabatic heat-up before reflood occurred during the test. The cladding temperatures at time of failure for MT4 range from 1077 to 1114 K, with peak internal gas pressures of approximately 8.9 to 9.3 MPa (initial value of 4.62 MPa), and gas pressures at failure of approximately 5.6 to 6.5 MPa. The average hoop strain in the experiments was noted at ~72 % with the maximum value reaching ~99 %.

A 2D axisymmetric geometry with 24 axial zones and 10 and 4 radial zones for the fuel and cladding, respectively, was used to simulate the full rod using Falcon. For OFFBEAT the mesh was divided into 100 axial cells and 16 and 4 radial cells for the fuel and cladding, respectively. The measured cladding temperature was provided as a time-dependent axial temperature profile to the cladding outer surface. The assumed axial power profile was provided as input. For the plastic-creep modelling in the Zircaloy cladding, the equation of state from the MATPRO v11 [47] for the high temperature regime (T>700 K) was used in Falcon. The failure criteria for cladding rupture in Falcon is based on the Cumulative Damage Index (CDI), which calculates the damage based on the displacement of the rod with time. Based on earlier validation studies on the Halden LOCA tests using Falcon [51], a threshold for CDI in the range 0.6–0.7 was considered for this simulation. For OFFBEAT, earlier trials showed that using the Erbacher high temperature creep model did not reach significant ballooning. The plasticity law from MATPRO, as in Falcon, already existed in OFFBEAT and it was modified to take the right expressions for the strain hardening exponent, strength coefficient and strain rate exponent from MATPRO. The results for the internal gas pressure and the cladding hoop strain along the length of the rod obtained using OFFBEAT and Falcon are shown in Figure 24, along with the experimental results. The gas pressures using the two codes show similar trends, however, the pressure increases for a longer duration in OFFBEAT, before decreasing. This trend is expected since as the ballooning begins, with the increasing volume, the gas pressure starts to decrease. The Falcon damage threshold is reached at ~ 54–56 s, at which the internal pressure is equated to the system pressure. In OFFBEAT, on the other hand, the simulation did not converge beyond t = 71 s. For the cladding hoop strain, OFFBEAT predicted 47.9 % strain as compared to 54.1 % (CDI=0.6) and 78.6 % (CDI=0.7) in Falcon. The hoop strain is still underpredicted in OFFBEAT, however it is a significant improvement over using the Erbacher creep model where the maximum hoop strain was found to be only ~18 %. A summary of the results from Falcon and OFFBEAT is presented in Table 7.

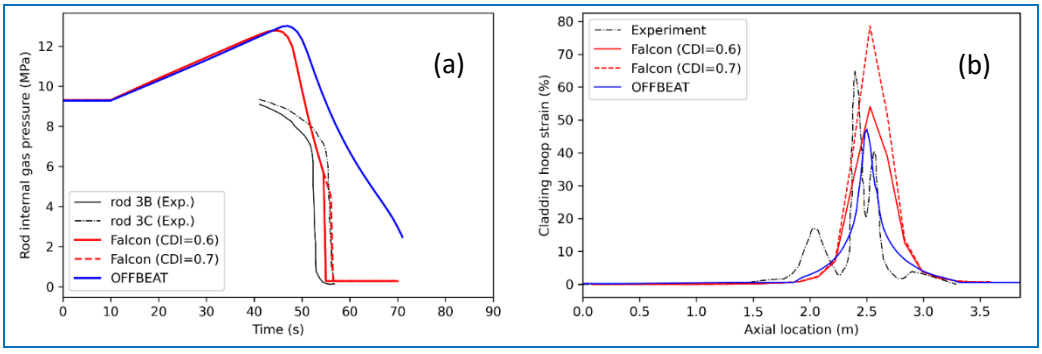

Figure 24 – Falcon *vs.* OFFBEAT comparison for (a) rod internal pressure, (b) cladding hoop strain, for the MT4 test rod.

	Experiment	Falcon (CDI =0.6)	Falcon (CDI =0.7)	OFFBEAT
Pressure (Max.)	8.9-9.3 MPa	12.78 MPa	12.78 MPa	13.01 MPa
Pressure (At rupture)	5.58-6.48 MPa	5.69 MPa	4.54 MPa	2.48 MPa*
Rupture time	52-58 s	54.5 s	56 s	71 s*
Hoop Strain	72 % (avg), 99 % (max)	54.07 %	78.63 %	47.91 %
Rupture location	2.68 m (avg)	2.53 m	2.53 m	2.50 m
				simulation crashed

Table 7 – Summary of Falcon and OFFBEAT results for the MT4 LOCA test.

5 Conclusions

This document presents the corpus of verification tests and studies performed within Task 5.1 for the three open-source advanced computational tools addressing the thermomechanical behaviour of nuclear fuel elements considered in the OperaHPC project, i.e.: the MMM mesoscale code, the multiscale meshless SPH method-based prototype tool, and the OFFBEAT engineering fuel rod scale code, coupled with the SCIANTIX code. These verification activities encompass comparison of computational results with analytical and/or manufactured solutions in simple configurations, as well as code-to-code comparison with existing advanced multidimensional fuel performance codes developed and/or used by OperaHPC partners on specific case studies consistent with the applications targeted in WP7 for which those codes are validated against experimental data.

In each of the three study cases tackled with MMM (viscoplasticity of polycrystalline UO_2, behaviour of a pressurized spherical bubble in an infinite elastic medium, viscoplasticity of a CERMET polycrystalline UO_2 with a chromium metallic interface), the comparison against Cast3M or analytical solutions (depending on the study case) has shown satisfying low relative errors.

The convergence results shown for the SPH prototype tool are considered acceptable as the method is not divergent. However, future development would need to implement methods to improve convergence rates in order to allow for more complex systems to be modelled with lower particle numbers.

So far not so numerous at the international level, the 2D-3D code-to-code benchmarks performed as part of Task 5.1 play a critical role in guiding the development of OFFBEAT. In particular, the comparison against ALCYONE and BISON on the K11-like rodlet PCMI case is highly valuable, as it highlights the differences between a 2D r–z approach and a 3D fragment-based approach and provides important insights into the impact of cracking models in the fuel pellet. These considerations are driving OFFBEAT towards the implementation of 3D fragment modelling and smeared cracking techniques, currently missing from the code. Similarly, the comparisons on LOCA tests (REBEKA and MT4) serve two purposes. On the one hand, they confirm the robustness of the current LOCA and large-strain models in OFFBEAT, as the results are consistent with Falcon and BISON (the latter as reported in the literature). On the other hand, the discrepancies observed with Falcon, particularly for MT4, might indicate the need for further investigation into creep and plasticity laws at high temperatures and a more detailed review of the large-strain formulation under conditions of significant deformation.

As regards SCIANTIX, the performed verification against manufactured solutions was used to assess the spatial-temporal convergence and the numerical accuracy of the spectral diffusion algorithm. The results of

this analysis demonstrate a more efficient selection of the spatial-temporal discretization parameters, allowing for a lower computational time without large penalization of the numerical accuracy, both in SCIANTIX (standalone) and OFFBEAT coupled with SCIANTIX.

The verification activities outlined in this document pertain to the key VVUQ&SA process towards the qualification of these tools for nuclear safety studies. They are to be considered together with the validation against experimental results, and uncertainty qualification and sensitivity analyses that will be presented respectively in deliverables D5.2 and D5.3 of the OperaHPC project.

References

1 OperaHPC project – Deliverable D4.1 – Best practices and QA protocols for code development, version 1, September 2023.

2 T. Helfer, G. Latu, R. Prat, M. Wangermez, F. Cuteri, MFEM/MGIS, a HPC mini-application targeting nonlinear thermo-mechanical simulations of nuclear fuels at mesoscale. Journal of Open Source Software, 10(108), 7719, 2025. https://doi.org/10.21105/joss.07719

3 OFFBEAT official GitLab repository, 2024. https://gitlab.com/foam-for-nuclear/offbeat

4 SCIANTIX official GitHub repository, 2024. https://github.com/sciantix/sciantix-official

5 https://github.com/thelfer/mfem-mgis

6 https://github.com/thelfer/tfel

7 https://mfem.org/

8 https://github.com/thelfer/MFrontGenericInterfaceSupport

9 OperaHPC project – Deliverable D9.2 - Detailed Work Plan for technical work Packages, version 1, August 2023.

10 https://github.com/rprat-pro/mm-opera-hpc

11 https://github.com/rprat-pro/mm-opera-hpc/blob/main/polycrystal/README.md

12 https://github.com/rprat-pro/mm-opera-hpc/blob/main/bubble/README.md

13 https://github.com/rprat-pro/mm-opera-hpc/blob/main/cermet/README.md

14 L. Portelette, J. Amodeo, R. Madec, J. Soulacroix, T. Helfer, B. Michel, 2018. Crystal viscoplastic modeling of UO_2 single crystal. Journal of Nuclear Materials 510, 635–643. https://doi.org/10.1016/j.jnucmat.2018.06.035

15 G. C. Ganzenmueller, SMOOTH MACH DYNAMICS. Fraunhofer Ernst-Mach Institute for High-Speed Dynamics.

16 R. Vacondio, C. Altomare, M. De Leffe *et al.* Grand challenges for Smoothed Particle Hydrodynamics numerical schemes. *Comp. Part. Mech.* 8, 575–588 (2021).

17 M. Horton, K. Travis, M. Bankhead, Developing smoothed particle methods for modelling continuum mechanical and thermal behaviour in nuclear fuel and cladding, PhD Thesis, University of Sheffield, 2022.

18 N. J. Quinlan, M. Basa, M. Lastiwka, 2006. Truncation error in mesh-free particle methods. International Journal for Numerical Methods in Engineering 66, 2064-2085. https://doi.org/10.1002/nme.1617

19 K. J. X. Sturm, E. L. Brunetto, S. Maccario, C. Fiorina, M. Hursin, A. Scolaro, On the Implementation of a Qualification Model for Nuclear Safety Codes, and its Application to the Verification & Validation of OFFBEAT, in Proc. TopFuel 2025, Nashville, TN, USA, Oct. 5–9, 2025.

20 ASN Guide No. 28, Qualification of scientific computing tools used in the nuclear safety case – 1st barrier. https://www.french-nuclear-safety.fr/asn-regulates/asn-guides/asn-guide-no.-28

21 International Fuel Performance Experiments (IFPE) Database, 2018, available at http://www.nea.fr/html/science/fuel/ifpelst.html

22 X. Su, M. Zhou, Analysis of shear stresses in tapered beams under bending, shear and axial force. Structures, 41 (2022) 849-865. https://doi.org/10.1016/j.istruc.2022.04.092

23 E. L. Brunetto, A. Scolaro, C. Fiorina, A. Pautz, Extension of the OFFBEAT fuel performance code to finite strains and validation against LOCA experiments, Nuclear Engineering and Design, Volume 406, 2023, 112232. https://doi.org/10.1016/j.nucengdes.2023.112232

24 P. Cardiff, Z. Tuković, P.D. Jaeger, M. Clancy, A. Ivanković, A Lagrangian cell-centred finite volume method for metal forming simulation. Int. J. Numer. Methods Eng. 109 (13), 2017, 1777–1803. https://doi.org/10.1002/nme.5345

25 A.R. Massih, Transformation kinetics of zirconium alloys under non-isothermal conditions, Journal of Nuclear Materials, Volume 384, Issue 3, 2009, 330-335. https://doi.org/10.1016/j.jnucmat.2008.11.033

26 G. Pastore, R.L. Williamson, R.J. Gardner, S.R. Novascone, J.B. Tompkins, K.A. Gamble, J.D. Hales, Analysis of fuel rod behavior during loss-of-coolant accidents using the BISON code: Cladding modeling developments and simulation of separate-effects experiments, Journal of Nuclear Materials, Volume 543, 2021, 152537. https://doi.org/10.1016/j.jnucmat.2020.152537

27 A. Scolaro, Development of a novel finite volume methodology for multi-dimensional fuel performance applications, PhD Thesis, EPFL, 2021. https://doi.org/10.5075/epfl-thesis-8822

28 A. Scolaro, I. Clifford, C. Fiorina, A. Pautz, The OFFBEAT multi-dimensional fuel behavior solver. Nuclear Engineering and Design, vol. 358, 110416, 2020. https://doi.org/10.1016/j.nucengdes.2019.110416

29 D. Pizzocri, T. Barani and L. Luzzi, SCIANTIX: A new open source multi-scale code for fission gas behaviour modelling designed for nuclear fuel performance codes. Journal of Nuclear Materials, 2020. 532: p. 152042. https://doi.org/10.1016/j.jnucmat.2020.152042

30 G. Zullo, D. Pizzocri, L. Luzzi, The SCIANTIX code for fission gas behaviour: Status, upgrades, separate-effect validation, and future developments, Journal of Nuclear Materials 587 (2023) 154744. https://doi.org/10.1016/j.jnucmat.2023.154744

31 A.H. Booth, A method of calculating fission gas diffusion from UO_2 fuel and its application to the X-2-f loop test, Canada, 1957.

32 M.V. Speight, A calculation on the migration of fission gas in material exhibiting precipitation and re-solution of gas atoms under irradiation, Nuclear Science and Engineering, 37(2), 1969,180-185. https://doi.org/10.13182/NSE69-A20676

33 K. Lassmann, H. Benk, Numerical algorithms for intragranular fission gas release. Journal of Nuclear Materials 280(2) (2000) 127–135. https://doi.org/10.1016/S0022-3115(00)00044-1

34 D. Pizzocri, C. Rabiti, L. Luzzi, T. Barani, P. Van Uffelen, G. Pastore, PolyPole-1: An accurate numerical algorithm for intra-granular fission gas release, Journal of Nuclear Materials 478 (2016) 333–342. https://doi.org/10.1016/j.jnucmat.2016.06.028

35 G. Pastore, D. Pizzocri, C. Rabiti, T. Barani, P. Van Uffelen, L. Luzzi, An effective numerical algorithm for intra-granular fission gas release during non-equilibrium trapping and resolution, Journal of Nuclear Materials 509 (2018) 687–699. https://doi.org/10.1016/j.jnucmat.2018.07.030

36 W.L. Oberkampf, T.G. Trucano, Verification and validation in computational fluid dynamics, Progress in Aerospace Sciences 38 (2002) 209–272. https://doi.org/10.1016/S0376-0421(02)00005-2

37 P.J. Roache, Code verification by the method of manufactured solutions, Journal of Fluids Engineering 124 (2002) 4–10. https://doi.org/10.1115/1.1436090

38 G. Zullo, D. Pizzocri, L. Luzzi, On the use of spectral algorithms for the prediction of short-lived volatile fission product release: Methodology for bounding numerical error, Nuclear Engineering and Technology 54 (2022) 1195–1205. https://doi.org/10.1016/j.net.2021.10.028

39 C. Introïni, I. Ramière, J. Sercombe, B. Michel, T. Helfer, J. Fauque, ALCYONE: the fuel performance code of the PLEIADES platform dedicated to PWR fuel rods behavior. Annals of Nuclear Energy, 2024. 207: p. 110711.

40 R.L. Williamson, J.D. Hales, S.R. Novascone, M.R. Tonks, D.R. Gaston, C.J. Permann, D. Andrs, R.C. Martineau, Multi-dimensional multiphysics simulation of nuclear fuel behavior. Journal of Nuclear Materials, 2012. 432: p. 149. https://mooseframework.inl.gov/releases/bison/v2.0.0, last accessed 02.06.2025.

41 M. Krstović, A. Scolaro, I. Guénot-Delahaie, A. Arkoma, B. Michel, M. Hursin, Code-to-code benchmarking of PCMI among high-fidelity fuel performance codes. In Proc. TopFuel 2025, October 5-9, 2025, Nashville, TN, USA.

42 J. Sercombe, B. Michel, C. Riglet-Martial, O. Fandeur, Modeling of Pellet Cladding Interaction. In Comprehensive Nuclear Materials: Second Edition, 2020. https://doi.org/10.1016/B978-0-12-803581-8.00715-3

43 Y. Rashid, R. Dunham, R. Montgomery, Fuel analysis and licensing code: FALCON MOD01, EPRI Report 1011308, 2004.

44 F.J. Erbacher, H.J. Neitzel, H. Rosinger, H. Schmidt, K. Wiehr, Burst criterion of Zircaloy fuel claddings in a loss-of-coolant accident, in Proc. of the Fifth Conference on Zirconium in the Nuclear Industry, ASTM, pp. 271-283, 1982.

45 M.E. Markiewicz, F. Erbacher, Experiments on ballooning in pressurized and transiently heated Zircaloy-4 tubes, Technical Report KfK 4343, Kernforschungszentrum Karlsruhe, Germany, 1988.

46 M. Limbäck, T. Andersson, A model for analysis of the effect of final annealing on the in- and out-of-reactor creep behavior of Zircaloy cladding, in ASTM Special Technical Publication, 1295, pp. 448-468, 1996.

47 D.L. Hagrman, G. A. Reyman, A handbook of materials properties for use in the analysis of light water reactor fuel rod behavior, MATPRO Version 11, in NUREG/CR-0497 (TREE-1280), US Nuclear Regulatory Commission (NRC), 1979.

48 G. Pastore, R.L. Williamson, R.J. Gardner, S.R. Novascone, J.B. Tompkins, K.A. Gamble, J.D. Hales, Analysis of fuel rod behavior during loss-of-coolant accidents using the BISON code: Cladding modeling developments and simulation of separate-effects experiments, Journal of Nuclear Materials vol. 543, 152537, 2021. https://doi.org/10.1016/j.jnucmat.2020.152537

49 L. Verma, I. Clifford, P. Konarski, A. Scolaro, H. Ferroukhi, OFFBEAT V&V studies for REBEKA tests on cladding ballooning and burst during LOCA conditions, Annals of Nuclear Energy, vol. 208, 110773, 2024. https://doi.org/10.1016/j.anucene.2024.110773

50 C. L. Wilson, C. L. Mohr, G. M. Hesson, N. J. Wildung, G. E. Russcher, B. J. Webb, M. D. Freshley, LOCA Simulation in NRU program: data report for the fourth materials experiment (MT-4), NUREG/CR-3272 (PNL-4669), Pacific Northwest Laboratory, Richland, WA 1983.

51 G. Khvostov, W. Wiesenack, B.C. Oberländer, E. Kolstad, G. Ledergerber, M. Zimmermann, Post-test analysis of the Halden LOCA experiment IFA-650.7 using the FALCON code, in Enlarged Halden Programme Group Meeting, Sandefjord, Norway, 2011.